

# Real-time Rendering-based Surgical Instrument Tracking via Evolutionary Optimization

Hanyang Hu<sup>1</sup>, Zekai Liang<sup>1</sup>, Florian Richter<sup>1</sup>, Michael C. Yip<sup>1</sup>, *Senior Member, IEEE*

**Abstract**—Accurate and efficient tracking of surgical instruments is fundamental for Robot-Assisted Minimally Invasive Surgery. Although vision-based robot pose estimation has enabled markerless calibration without tedious physical setups, reliable tool tracking for surgical robots still remains challenging due to partial visibility and specialized articulation design of surgical instruments. Previous works in the field are usually prone to unreliable feature detections under degraded visual quality and data scarcity, whereas rendering-based methods often struggle with computational costs and suboptimal convergence. In this work, we incorporate CMA-ES, an evolutionary optimization strategy, into a versatile tracking pipeline that jointly estimates surgical instrument pose and joint configurations. Using batch rendering to efficiently evaluate multiple pose candidates in parallel, the method significantly reduces inference time and improves convergence robustness. The proposed framework further generalizes to joint angle-free and bi-manual tracking settings, making it suitable for both vision feedback control and online surgery video calibration. Extensive experiments on synthetic and real-world datasets demonstrate that the proposed method significantly outperforms prior approaches in both accuracy and runtime. *The code and data will be released soon.*

## I. INTRODUCTION

Robot-assisted Minimally-Invasive Surgery (RMIS) has been increasingly adopted to improve surgical safety and procedural efficiency in complex, long-duration operations under physically demanding conditions. Accurate and efficient pose estimation of articulated surgical instruments is essential for a wide range of downstream applications, such as vision-based control [1], augmented reality guidance [2], and robot learning [3].

Uneven geometric structures, partial visibility of the kinematic chain, and noisy joint angle measurements caused by cable stretch introduce additional challenges for accurate articulated instrument pose recovery. Previous works have approached this problem from both kinematic calibration and pose calibration perspectives. Early works such as [4]–[8] proposed external sensing, including optical tracking and depth/vision systems, to compensate for kinematic error. However, these approaches require complex physical setups and are difficult to replicate or deploy in new environments. More recently, vision-based frameworks such as [9]–[11] have achieved markerless tool tracking by utilizing keypoint detection and a Perspective-n-Point (PnP) solver. [12] infused robot kinematic readings with 2D image-based feature detection to jointly estimate surgical instrument pose and

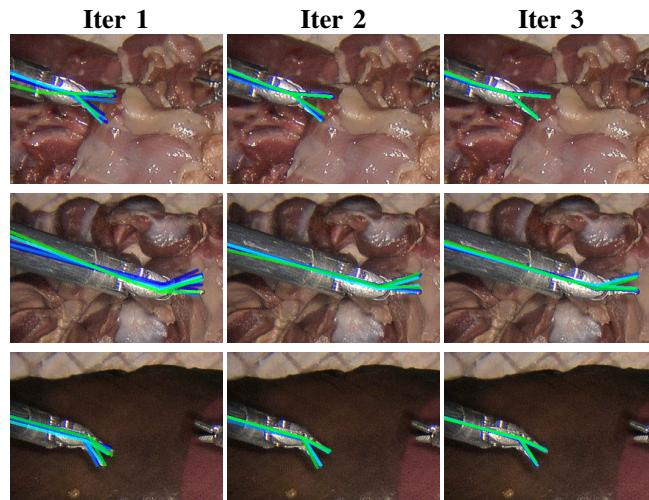


**Fig. 1:** Skeleton overlays of the top-5 CMA-ES samples across successive iterations. At each iteration, CMA-ES draws a population of candidate poses from a Gaussian distribution, evaluates their fitness using render-and-match objectives, and updates the distribution toward better solutions. Within 3 iterations, the sampled poses concentrate around the correct alignment.

kinematic calibration, formulating it as a lumped error. Nevertheless, vision-based feature detection, particularly keypoint detection, remains susceptible to noise and degradation under suboptimal endoscopic imaging conditions, making reliable pose initialization and stable tracking challenging. Liang *et al.* [13] first incorporated differentiable rendering into surgical instrument pose reconstruction as a more robust alternative to PnP-based approaches. Rendering-based frameworks [13]–[15] improve robustness and consistency by fully leveraging differentiable rendering matching in an iterative optimization manner, making them ideal for both single-frame pose reconstruction and kinematic calibration. However, they are computationally slow due to the iterative nature and prone to poor convergence, which limits their applicability in tracking setups with strict time constraints.

To address these limitations and fully leverage the potential of rendering-based approaches for real-time tracking under noisy kinematic measurements, we propose a novel framework based on evolutionary optimization that jointly estimates surgical instrument pose and joint angles. By leveraging the Covariance Matrix Adaptation Evolution Strategy (CMA-ES) [16], which evaluates multiple pose candidates in parallel (Fig. 1), the proposed method substantially reduces per-frame iterations and mitigates convergence to local minima, thereby outperforming differentiable rendering.

<sup>1</sup>Department of Electrical and Computer Engineering, University of California San Diego, La Jolla, CA 92093 USA. {hanyang-hu, z9liang, frichter, yip}@ucsd.edu

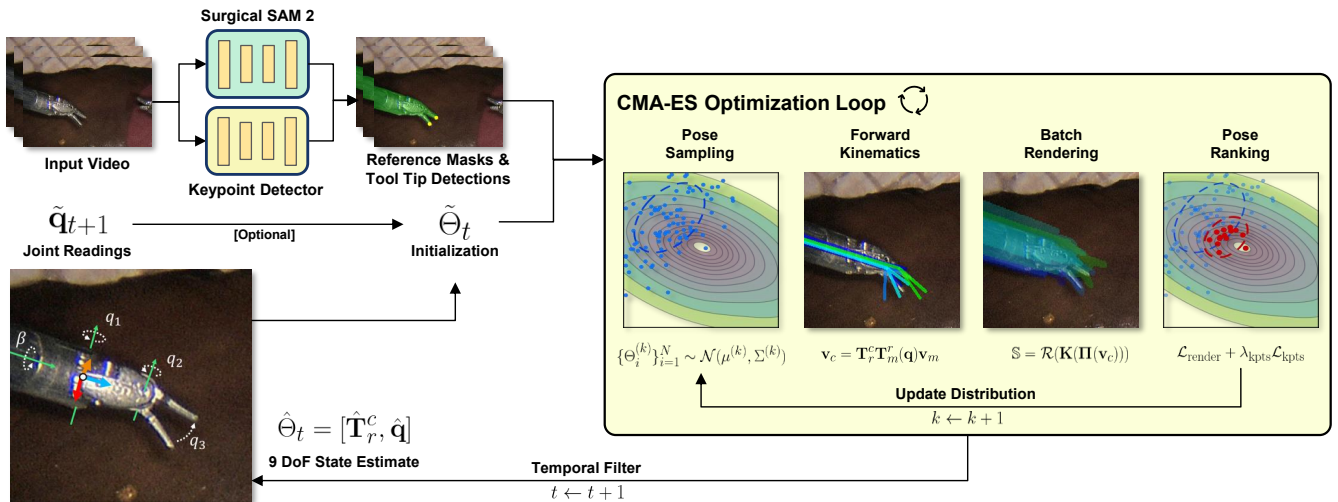


**Fig. 2: Overview of the proposed framework.** Given RGB video frames, segmentation masks and tool-tip detections are produced to define a render-and-match objective optimized via CMA-ES. At each iteration, pose candidates are sampled from the current distribution, evaluated in parallel through batched forward kinematics and rendering, and ranked by the objective to update the sampling distribution. The optimized estimates are temporally filtered and propagated to initialize the next frame. In this framework, three joint angles are optimized: wrist pitch  $q_1$ , wrist yaw  $q_2$ , and jaw angle  $q_3$ . The end-effector pose is defined at the wrist pitch frame. A look-at camera representation is adopted to decouple the shaft rotation  $\beta$  from the remaining rotational components.

Compared to prior online tracking methods, this framework achieves significant improvements in both accuracy and runtime with GPU-accelerated batch rendering and fitness evaluation. Furthermore, the framework is extended to handle joint angle-free and bi-manual setups, enabling the calibration of online surgical videos for surgical robot learning applications using only visual inputs.

The main contributions of this work are as follows:

- 1) A novel integrated online tracking framework that leverages CMA-ES, batch rendering, and temporal filtering to achieve robust real-time surgical instrument pose estimation from a monocular camera.
- 2) A tracking formulation that jointly calibrates instrument pose and kinematic measurements, and operates both with and without joint angle inputs, enabling both vision-based feedback control and online surgical video calibration.
- 3) An extension to bi-manual tracking that jointly optimizes two articulated instruments within a shared optimization framework, enabling efficient multi-tool tracking with modest computational overhead.

## II. RELATED WORK

Accurate tracking of articulated surgical robotic instruments remains challenging due to the limited observability of the long kinematic chain, noisy joint readings, and unconventional geometry, typically composed of two small articulated tips and a slender cylindrical shaft extending into the camera view. Early works focused on hardware-based or model-based compensation, including explicit cable-stretch modeling [17] and remote center of motion (RCM) calibration [18]. There were also approaches including [6], [7], [19], [20] that relied on external sensing systems or attached fiducial markers to estimate camera-to-robot transformations and

correct kinematic offsets from recorded trajectories. While these methods achieve accurate calibration under controlled conditions, they typically require additional hardware or labor-intensive calibration procedures, making them difficult to deploy and maintain in practical surgical workflows. In addition, physical marker detection is prone to motion blur and self-occlusion. These challenges have driven the recent development of markerless approaches that estimate instrument pose directly from monocular cameras.

Vision-based frameworks for robotic surgical tool tracking typically leverage deep neural networks to detect semantic visual features on the instrument and recover its pose using a PnP solver [21], [22]. However, for surgical robots such as da Vinci Research Kit (dVRK) [23], pose reconstruction must also account for inaccuracies in joint angle measurements induced by cable-driven transmission. To address this issue, Richter *et al.* [12] propose a unified framework that incorporates keypoint detections as observations while estimating a lumped error transformation, enabling simultaneous estimation of the pose and kinematic errors. Building upon this formulation, [24] further improves the observation model with deep learning-based cylinder detection. However, these approaches are often unreliable due to the poor endoscopic video quality. They are also limited by the scarcity of data with ground truth annotations.

More recently, rendering-based approaches have attracted increasing attention due to their consistency and robustness achieved through direct silhouette matching. Liang *et al.* [13] integrate geometric primitives with differentiable rendering-based optimization to enable robust single-shot calibration. Chen *et al.* [14] and Yang *et al.* [15] further apply differentiable rendering to recover surgical instrument trajectories from monocular videos. However, gradient-based optimization in these frameworks remains prone to local

minima and slow convergence. Although coarse sampling [13], [14] and image matching [15] strategies have been introduced to improve initialization, the overall optimization process is still computationally expensive. Consequently, existing rendering-based approaches are primarily deployed in offline settings.

### III. METHODOLOGY

An overview of the proposed pipeline is illustrated in Fig. 2, which estimates the 6-DoF pose and the visible joint angles of the surgical instrument with respect to the camera frame. Given RGB video frames, instrument segmentation masks are generated in real time using Surgical SAM 2 [25], while a learned keypoint detection network localizes the tool tips. These visual observations define a unified optimization objective over pose and joint parameters. The resulting optimization problem is solved using CMA-ES [16], an evolution strategy that iteratively refines a Gaussian search distribution over candidate states, with efficient objective evaluations carried out through batch rendering. A Kalman filter with a constant-velocity motion model is incorporated to enforce temporal consistency, and the filtered state is used to initialize the search distribution for the subsequent frame.

#### A. Surgical Instrument Tracking

This study considers the Patient Side Manipulator (PSM) equipped with a Large Needle Driver (LND) from the da Vinci® Surgical System. The manipulator has 6 DoF, along with an additional gripper angle. As shown in Fig. 2, the end-effector coordinate frame is defined at the wrist pitch frame (joint 4) of the PSM. Similar to prior works [13], [26], the surgical instrument localization is formulated as a nonlinear optimization problem over the end-effector pose  $\mathbf{T}_r^c \in SE(3)$ , together with the last three visible joint angles  $\mathbf{q} = [q_1, q_2, q_3]^\top \in \mathbb{R}^3$  corresponding to wrist pitch, wrist yaw, and gripper angle. For each RGB video frame  $\mathbb{I} \in \mathbb{R}^{H \times W \times 3}$ , the objective

$$\Theta^* = \arg \min_{\Theta} \mathcal{L}(\mathbb{I}, \Theta) \quad (1)$$

is to estimate the state  $\Theta = (\mathbf{T}_r^c, \mathbf{q})$  that minimizes the discrepancy between observed features from  $\mathbb{I}$  (e.g., segmentation masks and keypoints) and the reconstructions produced from the estimated state  $\Theta$ . After a single-shot calibration to initialize the solution, the state estimate from the previous frame is propagated to initialize optimization at the current frame. When joint angle readings are available, the measured values are used to initialize the optimization rather than relying on the propagated estimation.

1) *Evolutionary Optimization*: Rather than relying on gradient-based optimization, the Covariance Matrix Adaptation Evolution Strategy (CMA-ES) [16] is adopted. CMA-ES is a blackbox optimization method that iteratively refines a search distribution over the state space by maximizing the expected fitness  $J(\mu, \Sigma) := \mathbb{E}[-\mathcal{L}(\mathbb{I}, \Theta) \mid \mu, \Sigma]$ , leading to the optimal parameters

$$(\mu^*, \Sigma^*) = \arg \max_{\mu, \Sigma} J(\mu, \Sigma) \quad (2)$$

where  $\mu, \Sigma$  defines a Gaussian distribution over the state variable  $\Theta$ . This formulation effectively lifts the original objective  $\mathcal{L}(\mathbb{I}, \Theta)$  from the parameter level to the distribution level, such that the loss landscape with respect to the mean  $\mu$  approximates a Gaussian-smoothed version of  $\mathcal{L}(\mathbb{I}, \Theta)$ , improving robustness to local minima; and covariance adaptations enable rapid convergence to locally quadratic optima of the expected fitness  $J(\mu, \Sigma)$  [27].

A key advantage of CMA-ES in rendering-based pose estimation is its natural compatibility with blackbox batch rendering. At each iteration, the search distribution is updated based on the top- $M$  elite candidates  $\{\Theta_i^{(k)}\}_{i=1}^M$  of the  $N$  samples generated from the previous distribution  $\mathcal{N}(\mu^{(k)}, \Sigma^{(k)})$

$$\mu^{(k+1)} = \mu^{(k)} + c_m \sum_{i=1}^K w_i (\Theta_i^{(k)} - \mu^{(k)}), \quad (3)$$

$$\Sigma^{(k+1)} = (1 - c_1 - c_\mu) \Sigma^{(k)} + c_1 \mathbf{p}_c \mathbf{p}_c^\top + c_\mu \sum_{i=1}^K w_i \frac{\Theta_i^{(k)} - \mu^{(k)}}{\sigma_k} \left( \frac{\Theta_i^{(k)} - \mu^{(k)}}{\sigma_k} \right)^\top \quad (4)$$

where  $\{w_i\}_{i=1}^K$  are the weights of the elite candidates,  $c_m$ ,  $c_1$ , and  $c_\mu$  are learning rates,  $\mathbf{p}_c$  is the evolution path that accumulates successive steps of  $\mu$  to introduce momentum, and  $\sigma_k$  is the adapted step size. These updates depend only on the fitness ranking of sampled states, eliminating the need for differentiable rendering pipelines and enabling efficient parallel evaluation of multiple candidates in each iteration, substantially reducing the wall-clock time for pose estimation compared to gradient-based methods.

2) *Loss Function*: The objective function in (1) combines rendering loss as well as robust keypoint alignment loss to provide additional geometric constraints

$$\mathcal{L}(\mathbb{I}, \Theta) = \mathcal{L}_{\text{render}} + \lambda_{\text{kpts}} \mathcal{L}_{\text{kpts}} \quad (5)$$

where the rendering loss includes the Mean Squared Error (MSE) loss and the appearance loss [13], [26] to adjust the distance of the robot model

$$\mathcal{L}_{\text{render}}(\mathbb{M}_{\text{ref}}, \mathbb{S}) = \underbrace{\sum_{i=0}^{H-1} \sum_{j=0}^{W-1} (\mathbb{S}(i, j) - \mathbb{M}_{\text{ref}}(i, j))^2}_{\text{MSE loss}} + \lambda_{\text{app}} \underbrace{\left\| \sum_{i=0}^{H-1} \sum_{j=0}^{W-1} \mathbb{S}(i, j) - \mathbb{M}_{\text{ref}}(i, j) \right\|}_{\text{Appearance Loss}}. \quad (6)$$

The segmentation  $\mathbb{M}_{\text{ref}}$  is produced by Surgical SAM 2 [25] given the RGB image  $\mathbb{I}$ . The rendered mask  $\mathbb{S} \in \{0, 1\}^{H \times W}$  of the surgical tool is obtained from a blackbox renderer  $\mathcal{R}(\cdot)$  given the mesh vertices transformed to the camera frame

$$\mathbb{S} = \mathcal{R}(\mathbf{K}(\Pi(\mathbf{T}_r^c \mathbf{T}_m^r(\mathbf{q}) \mathbf{v}_m))) \quad (7)$$

where  $\mathbf{K} \in \mathbb{R}^{3 \times 3}$  is the camera intrinsic matrix,  $\Pi(\cdot)$  is the canonical projection,  $\mathbf{T}_m^r(\mathbf{q})$  is the forward kinematics transform from mesh frame to robot frame, and  $\mathbf{v}_m \in \mathbb{R}^{n \times 3}$  denotes the mesh vertices in the CAD mesh frame.

A heatmap-based 2D keypoint detection network with a ResNet-18 backbone is trained to localize the tool tips from the mask  $\mathcal{S}$ . Denoting the detected tool tips as  $\mathbf{t}_1^r, \mathbf{t}_2^r$  and the corresponding projected keypoints as  $\mathbf{t}_1^p, \mathbf{t}_2^p$  obtained from the pose candidates, the keypoint loss  $\mathcal{L}_{\text{kpts}}$  is given by

$$\mathcal{L}_{\text{kpts}}(\mathbf{t}^r, \mathbf{t}^p) = \min_{\sigma \in \{\{1,2\}, \{2,1\}\}} \sum_{i=1}^2 \left( \left\| \mathbf{t}_i^r - \mathbf{t}_{\sigma(i)}^p \right\|_2 - \tau \right)_+ + \left( \left\| \mathbf{t}_{\text{mean}}^r - \mathbf{t}_{\text{mean}}^p \right\|_2 - \tau \right)_+ \quad (8)$$

where  $(x)_+ = \max(0, x)$  is the positive-part operator and  $\tau > 0$  is a threshold that mitigates the effect of keypoint localization noise. The keypoint loss  $\mathcal{L}_{\text{kpts}}$  is evaluated only when exactly two distinct keypoints are decoded from the heatmap, ensuring robustness to corrupted segmentation masks that may cause missed tips or spurious detections.

3) *State Parameterization*: A unified rotation representation introduced by Liang *et al.* [13] is adopted for pose sampling within CMA-ES. Specifically, the look-at camera representation  $[\alpha, \beta, \gamma]^\top \in \mathbb{R}^3$  is used, such that

$$\mathbf{R}_{\text{LookAt}}(\alpha, \beta, \gamma) = \mathbf{R}_y(\gamma) \mathbf{R}_x(\alpha) \mathbf{R}_z(\beta), \quad (9)$$

where  $\mathbf{R}_x(\cdot)$ ,  $\mathbf{R}_y(\cdot)$ , and  $\mathbf{R}_z(\cdot)$  are rotations about the  $x$ -,  $y$ -, and  $z$ -axes, respectively. The pose transformation from the robot frame to the camera frame is defined as

$$\mathbf{T}_r^c(\alpha, \beta, \gamma, x, y, z) = \begin{bmatrix} \mathbf{R}_{\text{LookAt}}(\alpha, \beta, \gamma) & \mathbf{t} \\ \mathbf{0}^\top & 1 \end{bmatrix}, \quad (10)$$

where  $\mathbf{t} = [x, y, z]^\top \in \mathbb{R}^3$  is the translation vector. This formulation explicitly decouples the shaft rotation  $\beta$  from the remaining rotational components (Fig. 2), enabling structured pose sampling and accommodating the 180° rotational symmetry of instruments such as the Large Needle Driver.

In addition, joint angles are subject to physical box constraints, while CMA-ES does not natively support constrained optimization. Hard clamping or sigmoid-based mappings, although commonly used in gradient-based methods, can distort the sampling distribution and introduce bias toward boundary values when applied within the evolution strategy [28]. A cosine-based reparameterization is adopted to enforce the constraints while maintaining a well-behaved search distribution. Denoting the lower and upper bounds of the  $i$ -th joint angle as  $q_i^{\text{lb}}$  and  $q_i^{\text{ub}}$ , the mapping from a valid joint angle reading  $q_i \in [q_i^{\text{lb}}, q_i^{\text{ub}}]$  to an unconstrained representation  $\hat{q}_i$  for CMA-ES optimization is given by

$$\hat{q}_i = q_i^{\text{lb}} + \frac{q_i^{\text{ub}} - q_i^{\text{lb}}}{\pi} \arccos \left( 1 - 2 \frac{q_i - q_i^{\text{lb}}}{q_i^{\text{ub}} - q_i^{\text{lb}}} \right), \quad (11)$$

and the inverse mapping that recovers a valid joint angle  $q_i$  for fitness evaluation from the unconstrained variable  $\hat{q}_i$  is

$$q_i = q_i^{\text{lb}} + \frac{q_i^{\text{ub}} - q_i^{\text{lb}}}{2} \left( 1 - \cos \left( \pi \frac{\hat{q}_i - q_i^{\text{lb}}}{q_i^{\text{ub}} - q_i^{\text{lb}}} \right) \right). \quad (12)$$

This reparameterization guarantees that all CMA-ES samples respect the joint limits while maintaining an unconstrained search distribution internally.

4) *Temporal Filtering*: A temporal filter is applied to the state estimates to reduce optimization-induced jitter and mitigate noise from segmentation masks and keypoint detection. Specifically, the filter is defined as  $\mathbf{s}_t = [\Theta_t, \dot{\Theta}_t]^\top \in \mathbb{R}^{18}$ , where the 9-DoF state  $\Theta_t$  encodes the pose and joint angles, and  $\dot{\Theta}_t \in \mathbb{R}^9$  their corresponding velocities. The motion model assumes constant velocity

$$\mathbf{s}_t = \begin{bmatrix} \mathbf{I} & \Delta t \mathbf{I} \\ \mathbf{0} & \mathbf{I} \end{bmatrix} \mathbf{s}_{t-1} + \mathbf{w}_t, \quad \mathbf{w}_t \sim \mathcal{N}(\mathbf{0}, \mathbf{Q}), \quad (13)$$

where  $\mathbf{I}, \mathbf{0}$  denote the identity and zero matrices,  $\Delta t$  is the time interval between frames,  $\mathbf{w}_t$  is the process noise, and  $\mathbf{Q} \in \mathbb{R}^{18 \times 18}$  is the process noise covariance. Furthermore, estimates from CMA-ES optimization serve as direct observations  $\mathbf{z}_t$  of the state

$$\mathbf{z}_t = [\mathbf{I} \ \mathbf{0}] \mathbf{s}_t + \mathbf{v}_t, \quad \mathbf{v}_t \sim \mathcal{N}(\mathbf{0}, \mathbf{R}), \quad (14)$$

where  $\mathbf{v}_t$  is the observation noise and  $\mathbf{R} \in \mathbb{R}^{9 \times 9}$  is the measurement noise covariance. Filtered joint angles are clamped to their physical limits to ensure valid configurations.

## B. Bi-Manual Tracking

To extend the proposed framework to bi-manual tracking setups, the state parameters for both arms are jointly optimized as a concatenated parameter  $\Theta = [\Theta_L, \Theta_R]^\top \in \mathbb{R}^{18}$ , where  $\Theta_L, \Theta_R \in \mathbb{R}^9$  represent the 9-DoF state of the left and right arms. In this formulation, both arms are rendered jointly, and the rendering loss (6) is evaluated on the combined image. The overall objective is then defined as:

$$\mathcal{L}(\mathbb{I}, \Theta) = \mathcal{L}_{\text{render}} + \lambda_{\text{kpts}} (\mathcal{L}_{\text{kpts}}^L + \mathcal{L}_{\text{kpts}}^R), \quad (15)$$

where  $\mathcal{L}_{\text{kpts}}^L$  and  $\mathcal{L}_{\text{kpts}}^R$  denote the keypoint losses for the left and right arms, respectively.

Inspired by separable CMA-ES [29], we constrain the covariance update (4) in CMA-ES to a block-diagonal form:

$$\Sigma^{(k)} = \begin{bmatrix} \Sigma_L^{(k)} & \mathbf{0} \\ \mathbf{0} & \Sigma_R^{(k)} \end{bmatrix}, \quad (16)$$

so that the evolution of each arm's state is governed independently by its own covariance block  $\Sigma_L^{(k)}, \Sigma_R^{(k)} \in \mathbb{R}^{9 \times 9}$ . This design reduces model complexity and prevents spurious correlations between the states of the two arms.

## IV. EXPERIMENTS

### Implementation Setups

All experiments are conducted on a workstation equipped with an NVIDIA RTX 4090 GPU and an AMD Ryzen 9 9960X CPU. Reference segmentation masks used in the tracking pipeline are generated by Surgical SAM 2 [25] with point prompts provided in the first frame of the trajectory. The optimization frameworks are implemented with EvoTorch [30] and NvDiffRast [31]. For evolutionary optimization, gradients are not evaluated, and instance-mode batch rendering is used for GPU-parallelized evaluation of the generated samples in each iteration.

For initialization, the pose-ranking method of Liang *et al.* [13] is adapted to enable a fully joint angle-free pipeline. In

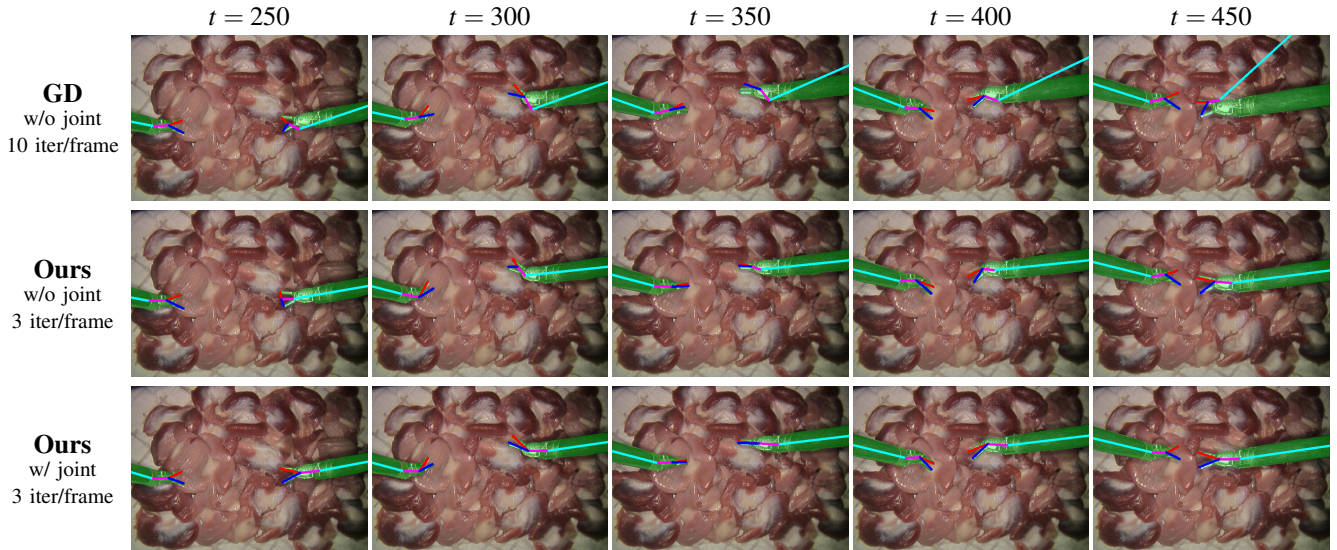


**Fig. 3:** Qualitative comparison of bi-manual tracking on the SurgPose dataset. Reference masks are shown with green overlays. The proposed method achieves accurate pose reconstruction when joint angle readings are available and remains robust to poor initialization even without joint measurements, while the gradient-based approach is prone to local minima and error accumulation.

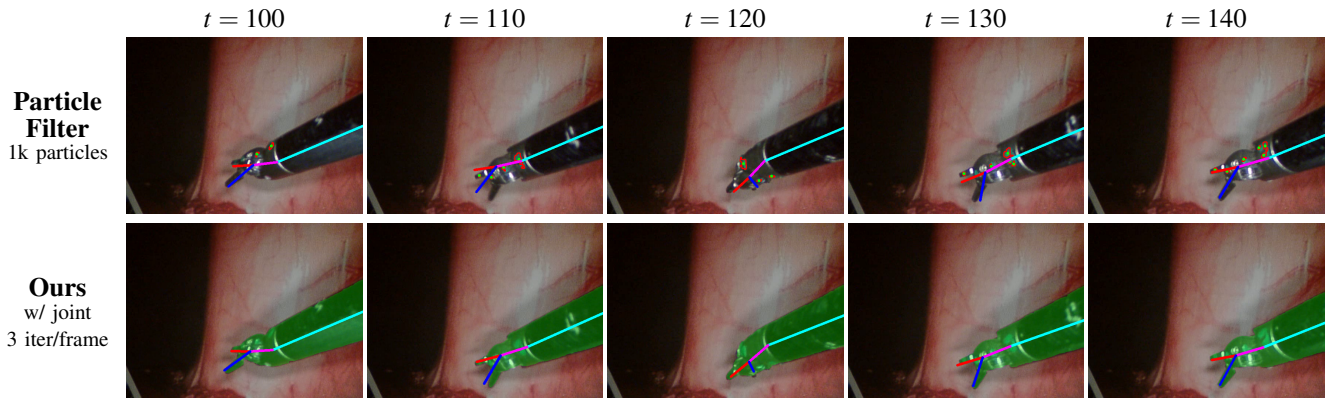


**Fig. 4:** Qualitative comparison of single-arm tracking on the collected dataset. Detected colored markers for the particle filter are shown as green dots (centroids of the regions outlined by red contours). Reference masks for the proposed approach are shown with green overlays. Our method demonstrates improved accuracy in the alignment of tool tips compared to the particle filter.

addition to the original pose hypothesis space, initial joint configurations are also sampled from a feasible set. Instead of uniformly sampling this expanded search space, TuRBO [32] is applied to adaptively concentrate exploration on promising regions, thereby improving efficiency despite the increased dimensionality introduced by the additional joint variables.

During tracking, the parameter space is normalized to account for heterogeneous units and magnitudes. CMA-ES is initialized with covariance  $\Sigma^{(0)} = \mathbf{I}$ , and the default learning rates  $c_m$  and  $c_\mu$  are increased to accelerate convergence, with  $N = 70$  samples generated per iteration. The Adam optimizer [33] with a learning rate of 0.1 in the normalized space serves as a gradient-based baseline.

#### Synthetic Dataset

To quantitatively evaluate the pose reconstruction accuracy, 16 pairs of synthetic trajectories (left and right arms) are generated. Each pair consists of 1000 frames and is constructed by selecting 20 feasible waypoints and interpolating between them using cubic Hermite splines. The

trajectories are then perturbed with temporally correlated noise via an Ornstein-Uhlenbeck process and smoothed with a low-pass filter. Corresponding binary masks are rendered at a resolution of  $700 \times 493$ . To simulate realistic segmentation errors, the masks are further perturbed with random dilation, erosion, and edge blobs. Additionally, 10,000 synthetic masks are generated from the pose hypothesis space to train the keypoint detector.

#### Real-world Dataset

For real-world evaluation, 12 trajectories from the SurgPose dataset [34] are selected, with both manipulators equipped with Large Needle Drivers (LND). The dataset is divided into 8 sequences with nominal speed and 4 sequences exhibiting rapid movements. In addition, we collected 6 trajectories of synchronized left and right stereo image streams at  $640 \times 480$  with painted markers and joint angle readings to benchmark against the online tool tracking method proposed by Richter *et al.* [12], which relies on colored markers on the instrument for keypoint detection and applies a particle filter

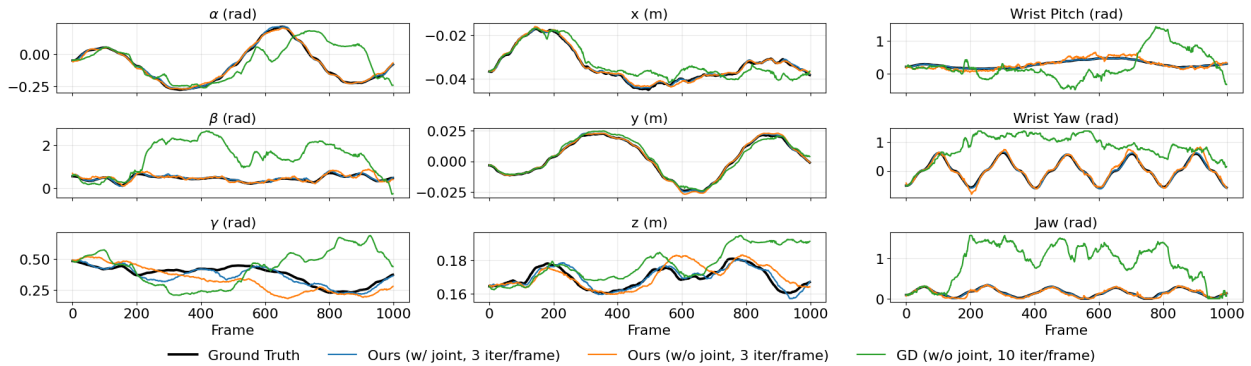


**Fig. 5:** Qualitative comparison of pose reconstruction results using different optimization strategies on a synthetic trajectory.

to estimate the lumped error transform. The collected dataset also includes refined segmentation masks to enable more accurate quantitative evaluation. The recorded trajectories vary in length from 250 to 554 frames, with an average of 436 frames per sequence. For the fast-motion trajectories in SurgPose and in the collected dataset, the process noises of the velocity term in the Kalman filter motion model (13) are correspondingly increased to better accommodate larger inter-frame velocity deviations.

#### A. Qualitative Results.

The qualitative tracking results are shown in Fig. 3 and Fig. 4, illustrating the accuracy and robustness of different tracking strategies on both the SurgPose dataset and the collected dataset. On the SurgPose dataset (Fig. 3), the proposed method is compared against the gradient-based baseline for bi-manual tracking. Gradient descent suffers from stagnation in local optima, which leads to error accumulation and visible drift over time. In contrast, CMA-ES demonstrates stronger robustness to early tracking errors (e.g., at Frame 250) even without joint angle readings. Furthermore, the tracking becomes more accurate when joint angle readings are incorporated, producing consistent alignment between the estimated pose and image observations across frames. Figure 4 presents the comparison with the particle filter baseline of Richter *et al.* [12] on the collected dataset. Using 1000 particles as in their original configuration, the particle filter shows noticeable misalignment at the tool tips. In contrast, the proposed method achieves more accurate alignment while maintaining smoother and more stable tracking.

On the synthetic dataset (Fig. 5), the estimated rotation, translation, and joint trajectories are compared against ground truth. CMA-ES with joint angle readings achieves the most accurate reconstruction across all components, closely matching the reference motion throughout the sequence. Even without joint measurements, the proposed method maintains stable and well-aligned estimates, consistently outperforming the gradient-based baseline. In contrast, gradient descent exhibits noticeable deviations, particularly in rotation and joint angle trajectories, reflecting its sensitivity to local minima and reduced robustness over time.

#### B. Quantitative Results.

Table I reports the quantitative results on the synthetic dataset and the SurgPose dataset. The proposed framework based on CMA-ES is compared against gradient descent (GD) baselines and XNES [27], a natural evolution strategy closely related to CMA-ES. In gradient-based ablations, NvDiffRast is replaced with PyTorch3D [35], as used in prior works [13], [26].

For the synthetic dataset with ground-truth kinematics data, pose reconstruction accuracy is evaluated in terms of rotation, translation, and joint angle errors. Rotation error is computed as  $\|\log(\mathbf{R}^T \hat{\mathbf{R}})^V\|_2$ , where  $\mathbf{R}$  and  $\hat{\mathbf{R}}$  denote the ground-truth and estimated orientations, respectively. Translation error is measured as the  $\ell_2$  distance, and absolute errors are reported for the three visible joints: wrist pitch  $q_1$ , wrist yaw  $q_2$ , and jaw angle  $q_3$ . To resolve the pose ambiguity of LND, the pose with the smaller absolute error in the local  $z$ -axis rotation  $\beta$  is selected among the two equivalent solutions for evaluation.

For the SurgPose dataset, raw joint angle readings require compensation and cannot serve as direct ground truth. Therefore, the Intersection-over-Union (IoU) between the reference mask  $\mathbb{M}_{\text{ref}}$  from Surgical SAM 2 and the rendered mask  $\mathbb{S}$  from the pose estimation is computed, and the mask error is defined as  $1 - \text{IoU}(\mathbb{M}_{\text{ref}}, \mathbb{S})$ . When ground-truth reference keypoints  $\mathbf{t}'$  are available, the reprojection error is computed as the sum of  $\ell_2$  distances between corresponding keypoints. For fair comparison, we use pre-computed reference masks  $\mathbb{M}_{\text{ref}}$  for all methods. To demonstrate end-to-end performance, we additionally include a fully online variant of our approach, where segmentation masks are generated by Surgical SAM 2 on the fly.

Across both single- and dual-arm tracking, CMA-ES achieves the best balance between accuracy and efficiency. With only 3 iterations per frame, it consistently outperforms GD with 10–20 iterations in pose reconstruction for both the synthetic and real-world data while requiring approximately 37% of the runtime. Incorporating joint angle readings further improves performance and yields the best overall results. Although XNES is more efficient than GD, it remains inferior to CMA-ES in reconstruction accuracy, as the CMA-ES update rule (4) enables faster convergence to local quadratic optima [27]. Substituting NvDiffRast with PyTorch3D in the

Optimizer	Setup		Speed Time (ms)	Synthetic Data					SurgPose			
	Joint	Iters		Rot.	Trans.	$q_1$	$q_2$	$q_3$	Normal Mask Err.	KP Err.	Fast Mask Err.	KP Err.
<b>Single-Arm Tracking</b>												
GD (NvDiffRast)	✓	10	42.40	0.4957	0.0089	0.3378	0.3377	0.1715	0.1432	8.8057	0.2650	8.5244
		10	42.51	0.2383	0.0052	<u>0.0326</u>	<u>0.0353</u>	<b>0.0028</b>	0.0975	7.2869	0.2052	10.2803
		20	79.53	0.2830	0.0053	0.2051	0.1479	0.0601	0.0993	7.9207	0.2692	9.2774
GD (PyTorch3D)		10	98.59	0.5279	0.0108	0.4162	0.2571	0.0501	0.1445	8.4748	0.2306	8.8919
XNES		3	<u>15.45</u>	0.4565	0.0075	0.2526	0.2977	0.1397	0.0913	6.7764	0.1417	7.5942
CMA-ES (Ours)	✓	3	15.93	0.2136	0.0032	0.1371	0.1335	0.0705	0.0729	<u>5.7210</u>	0.1107	<u>6.9970</u>
		3	15.85	<b>0.0550</b>	<b>0.0015</b>	<b>0.0066</b>	<b>0.0144</b>	<u>0.0043</u>	0.0757	6.1491	0.1066	7.3529
		5	23.90	<u>0.0734</u>	<b>0.0015</b>	0.0518	0.0535	0.0241	<u>0.0674</u>	<b>5.1007</b>	<b>0.0931</b>	<b>6.3607</b>
CMA-ES (Online)	✓	3	25.15*	–	–	–	–	–	<b>0.0662</b>	6.0133	<u>0.1004</u>	7.1115
CMA-ES (w/o kpt. loss)		3	15.77	0.2356	<u>0.0028</u>	0.1279	0.2015	0.1444	0.0727	14.9398	0.1020	24.5069
CMA-ES (OpenCV kpt.)		3	<b>13.63</b>	0.7706	0.0177	0.6312	0.9356	0.7557	0.0998	9.9159	0.1484	12.5161
<b>Dual-Arm Tracking</b>												
GD	✓	10	57.46	0.5169	0.0093	0.3412	0.3336	0.1897	0.1545	10.4062	0.2739	9.7430
		10	57.52	<u>0.1943</u>	<u>0.0055</u>	<u>0.0341</u>	<u>0.0351</u>	<b>0.0029</b>	<u>0.0924</u>	<u>6.8002</u>	0.1914	9.3923
CMA-ES	✓	3	<u>21.69</u>	0.5068	0.0090	0.2999	0.3753	0.1959	0.1004	6.8037	<u>0.1625</u>	<u>8.1210</u>
		3	<b>21.68</b>	<b>0.1736</b>	<b>0.0049</b>	<b>0.0128</b>	<b>0.0221</b>	<u>0.0047</u>	<b>0.0832</b>	<b>6.0193</b>	<b>0.1268</b>	<b>7.1138</b>

**TABLE I:** Quantitative results and ablations on the synthetic dataset and the SurgPose dataset. Except for the online version, the reference masks are pre-computed using Surgical SAM 2. **Setup:** “Joint” indicates whether joint angle readings are used, and “Iters” denotes the number of iterations per frame. Runtimes report the per-frame inference latency (ms) for optimization; for the online version of our method, the runtime marked with an asterisk includes Surgical SAM 2 inference. Rotation and joint angle errors are reported in radians (rad), translation error in meters (m), mask error as  $1 - \text{IoU}$ , and keypoint reprojection error in pixels. For dual-arm tracking, each arm is evaluated separately, and results are averaged across the two arms. Best results are in **bold** and second-best are underlined, respectively.

Method	Mask Err.	FPS
Richter <i>et al.</i> (1k particles) [12]	$0.2476 \pm 0.0515$	$19.22 \pm 0.45$
Ours (w/ joint, 3 iter/frame)	$0.1177 \pm 0.0396$	$43.34 \pm 1.61$

**TABLE II:** Comparison of online tracking accuracy and inference speed between Richter *et al.* [12] and the proposed method. All values are reported as mean  $\pm$  std. For the proposed method, the reported FPS includes both Surgical SAM 2 inference and subsequent CMA-ES optimization time.

gradient-based setting results in both reduced accuracy and increased runtime. Furthermore, the contribution of the keypoint loss  $\mathcal{L}_{\text{kpts}}$  in (8) is assessed through two ablations: (1) removing the keypoint term slightly degrades performance, while (2) replacing the trained keypoint detection model with the traditional GoodFeaturesToTrack method [36] yields the worst overall performance, underscoring the importance of robust keypoint supervision.

Table II reports the quantitative results of benchmarking the proposed method against the particle filters proposed by Richter *et al.* [12] for online tool tracking on the collected dataset. The mask error ( $1 - \text{IoU}$ ) and inference speed (FPS) are reported for both methods. For the proposed method, the FPS accounts for both Surgical SAM 2 prediction and CMA-ES optimization. The method demonstrates clear improvements in both accuracy and efficiency, benefiting from a GPU-parallelized implementation.

## V. DISCUSSIONS AND CONCLUSIONS

In this work, we present a robust and generalizable real-time surgical instrument tracking framework based on

evolutionary optimization and batched rendering. Through extensive qualitative and quantitative evaluations on both synthetic and real-world datasets, we demonstrate that the proposed approach effectively addresses key limitations of prior methods, including noisy joint angle readings, suboptimal convergence, and long iterative optimization. These improvements in accuracy and runtime performance enhance its practicality for downstream clinical and robotic applications.

A remaining limitation of rendering-based methods lies in their dependence on accurate segmentation. Errors caused by occlusion or noisy segmentation propagate directly to pose and kinematic estimation. Furthermore, the SurgPose dataset does not contain sequences with overlapping instruments, preventing evaluation of our bi-manual tracking method under frequent instrument–instrument occlusions encountered in real surgical procedures. In future work, we will incorporate more robust instrument-level segmentation strategies to better handle occlusion scenarios. We also plan to leverage high-throughput batch rendering platforms (e.g., [37]) to fully exploit the blackbox optimization paradigm of evolutionary strategies and further improve computational scalability.

## REFERENCES

- [1] C. Molnár, T. D. Nagy, R. N. Elek, and T. Haidegger, “Visual servoing-based camera control for the da vinci surgical system,” in *2020 IEEE 18th International Symposium on Intelligent Systems and Informatics (SISY)*, 2020, pp. 107–112.
- [2] M. Kalia, A. Avinash, N. Navab, and S. Salcudean, “Preclinical evaluation of a markerless, real-time, augmented reality guidance system for robot-assisted radical prostatectomy,”

- International Journal of Computer Assisted Radiology and Surgery*, vol. 16, no. 7, p. 1181–1188, Jun. 2021. [Online]. Available: <http://dx.doi.org/10.1007/s11548-021-02419-9>
- [3] J. W. Kim, T. Z. Zhao, S. Schmidgall, A. Deguet, M. Kobilarov, C. Finn, and A. Krieger, “Surgical robot transformer (srt): Imitation learning for surgical tasks,” 2024. [Online]. Available: <https://arxiv.org/abs/2407.12998>
  - [4] D. Zhang, Z. Li, K. Chen, J. Xiong, X. Zhang, and L. Wang, “An optical tracker based robot registration and servoing method for ultrasound guided percutaneous renal access,” *Biomedical engineering online*, vol. 12, no. 1, p. 47, 2013.
  - [5] C. Jun, R. Decker, and D. Stoianovici, “Using optical tracking for kinematic testing of medical robots,” *The International Journal of Medical Robotics and Computer Assisted Surgery*, vol. 14, no. 2, p. e1890, 2018.
  - [6] D. Seita, S. Krishnan, R. Fox, S. McKinley, J. Canny, and K. Goldberg, “Fast and reliable autonomous surgical debridement with cable-driven robots using a two-phase calibration procedure,” in *2018 IEEE International Conference on Robotics and Automation (ICRA)*, 2018, pp. 6651–6658.
  - [7] M. Hwang, D. Seita, B. Thananjeyan, J. Ichnowski, S. Paradis, D. Fer, T. Low, and K. Goldberg, “Applying depth-sensing to automated surgical manipulation with a da vinci robot,” in *2020 International Symposium on Medical Robotics (ISMR)*, 2020, pp. 22–29.
  - [8] O. Özgüner, T. Shkurti, S. Huang, R. Hao, R. C. Jackson, W. S. Newman, and M. C. Çavuşoğlu, “Camera-robot calibration for the da vinci robotic surgery system,” *IEEE Transactions on Automation Science and Engineering*, vol. 17, no. 4, pp. 2154–2161, 2020.
  - [9] Y. Li, F. Richter, J. Lu, E. K. Funk, R. K. Orosco, J. Zhu, and M. C. Yip, “Super: A surgical perception framework for endoscopic tissue manipulation with surgical robotics,” *IEEE Robotics and Automation Letters*, vol. 5, no. 2, pp. 2294–2301, 2020.
  - [10] S. Lin, A. J. Miao, J. Lu, S. Yu, Z.-Y. Chiu, F. Richter, and M. C. Yip, “Semantic-super: A semantic-aware surgical perception framework for endoscopic tissue identification, reconstruction, and tracking,” in *2023 IEEE International Conference on Robotics and Automation (ICRA)*, 2023, pp. 4739–4746.
  - [11] J. Lu, A. Jayakumari, F. Richter, Y. Li, and M. C. Yip, “Super deep: A surgical perception framework for robotic tissue manipulation using deep learning for feature extraction,” in *2021 IEEE International Conference on Robotics and Automation (ICRA)*, 2021, pp. 4783–4789.
  - [12] F. Richter, J. Lu, R. K. Orosco, and M. C. Yip, “Robotic tool tracking under partially visible kinematic chain: A unified approach,” *IEEE Transactions on Robotics*, vol. 38, no. 3, pp. 1653–1670, 2022.
  - [13] Z. Liang, Z.-Y. Chiu, F. Richter, and M. C. Yip, “Differentiable rendering-based pose estimation for surgical robotic instruments,” in *2025 IEEE/RSJ International Conference on Intelligent Robots and Systems (IROS)*. IEEE, 2025, pp. 20 898–20 905.
  - [14] J.-T. Chen, X. Chen, J. W. Kim, P. M. Scheikl, R. J. Cha, and A. Krieger, “Surgipose: Estimating surgical tool kinematics from monocular video for surgical robot learning,” in *2025 IEEE/RSJ International Conference on Intelligent Robots and Systems (IROS)*. IEEE, Oct. 2025, p. 20912–20919. [Online]. Available: <http://dx.doi.org/10.1109/IROS60139.2025.11247452>
  - [15] S. Yang, Z. Wu, M. Hong, Q. Li, D. Shen, S. E. Salcudean, and Y. Jin, “Instrument-Splatting: Controllable Photorealistic Reconstruction of Surgical Instruments Using Gaussian Splatting,” in *proceedings of Medical Image Computing and Computer Assisted Intervention – MICCAI 2025*, vol. LNCS 15962. Springer Nature Switzerland, September 2025.
  - [16] N. Hansen and A. Ostermeier, “Completely derandomized self-adaptation in evolution strategies,” *Evol. Comput.*, vol. 9, no. 2, pp. 159–195, 2001.
  - [17] M. Miyasaka, J. Matheson, A. Lewis, and B. Hannaford, “Measurement of the cable-pulley coulomb and viscous friction for a cable-driven surgical robotic system,” in *2015 IEEE/RSJ International Conference on Intelligent Robots and Systems (IROS)*, 2015, pp. 804–810.
  - [18] F. Zhong, Z. Wang, W. Chen, K. He, Y. Wang, and Y.-H. Liu, “Hand-eye calibration of surgical instrument for robotic surgery using interactive manipulation,” *IEEE Robotics and Automation Letters*, vol. 5, no. 2, pp. 1540–1547, 2020.
  - [19] M. Hwang, B. Thananjeyan, S. Paradis, D. Seita, J. Ichnowski, D. Fer, T. Low, and K. Goldberg, “Efficiently calibrating cable-driven surgical robots with rgbd fiducial sensing and recurrent neural networks,” *IEEE Robotics and Automation Letters*, vol. 5, no. 4, pp. 5937–5944, 2020.
  - [20] B. Wu, L. Wang, X. Liu, L. Wang, and K. Xu, “Closed-loop pose control and automated suturing of continuum surgical manipulators with customized wrist markers under stereo vision,” *IEEE Robotics and Automation Letters*, vol. 6, no. 4, pp. 7137–7144, 2021.
  - [21] J. Lambrecht and L. Kästner, “Towards the usage of synthetic data for marker-less pose estimation of articulated robots in rgb images,” in *2019 19th International Conference on Advanced Robotics (ICAR)*, 2019, pp. 240–247.
  - [22] J. Lambrecht, “Robust few-shot pose estimation of articulated robots using monocular cameras and deep-learning-based keypoint detection,” in *2019 7th International Conference on Robot Intelligence Technology and Applications (RiTA)*, 2019, pp. 136–141.
  - [23] P. Kazanzides, Z. Chen, A. Deguet, G. S. Fischer, R. H. Taylor, and S. P. DiMaio, “An open-source research kit for the da vinci® surgical system,” in *2014 IEEE International Conference on Robotics and Automation (ICRA)*, 2014, pp. 6434–6439.
  - [24] C. D’Ambrosia, F. Richter, Z.-Y. Chiu, N. Shinde, F. Liu, H. I. Christensen, and M. C. Yip, “Robust surgical tool tracking with pixel-based probabilities for projected geometric primitives,” in *2024 IEEE International Conference on Robotics and Automation (ICRA)*, 2024, pp. 15 455–15 462.
  - [25] H. Liu, E. Zhang, J. Wu, M. Hong, and Y. Jin, “Surgical sam 2: Real-time segment anything in surgical video by efficient frame pruning,” 2024. [Online]. Available: <https://arxiv.org/abs/2408.07931>
  - [26] J. Lu, F. Liu, C. Girerd, and M. C. Yip, “Image-based pose estimation and shape reconstruction for robot manipulators and soft, continuum robots via differentiable rendering,” in *2023 IEEE International Conference on Robotics and Automation (ICRA)*, 2023, pp. 560–567.
  - [27] T. Glasmachers, T. Schaul, S. Yi, D. Wierstra, and J. Schmidhuber, “Exponential natural evolution strategies,” in *Proceedings of the 12th Annual Conference on Genetic and Evolutionary Computation*, ser. GECCO ’10. New York, NY, USA: Association for Computing Machinery, 2010, p. 393–400. [Online]. Available: <https://doi.org/10.1145/1830483.1830557>
  - [28] F. Caraffini, A. V. Kononova, and D. Corne, “Infeasibility and structural bias in differential evolution,” *Information Sciences*, vol. 496, pp. 161–179, 2019.
  - [29] R. Ros and N. Hansen, “A simple modification in cma-es achieving linear time and space complexity,” in *Parallel Problem Solving from Nature – PPSN X*, G. Rudolph, T. Jansen, N. Beume, S. Lucas, and C. Poloni, Eds. Berlin, Heidelberg: Springer Berlin Heidelberg, 2008, pp. 296–305.
  - [30] N. E. Toklu, T. Atkinson, V. Micka, P. Liskowski, and R. K. Srivastava, “Evotorch: Scalable evolutionary computation in python,” 2023. [Online]. Available: <https://arxiv.org/abs/2302.12600>
  - [31] S. Laine, J. Hellsten, T. Karras, Y. Seol, J. Lehtinen, and T. Aila, “Modular primitives for high-performance differentiable rendering,” *ACM Transactions on Graphics*, vol. 39, no. 6, 2020.
  - [32] D. Eriksson, M. Pearce, J. Gardner, R. D. Turner, and M. Poloczek, “Scalable global optimization via local Bayesian optimization,” in *Advances in Neural Information Processing Systems*, 2019, pp. 5496–5507. [Online]. Available: <http://papers.nips.cc/paper/8788-scalable-global-optimization-via-local-bayesian-optimization.pdf>
  - [33] D. P. Kingma and J. Ba, “Adam: A method for stochastic optimization,” 2017. [Online]. Available: <https://arxiv.org/abs/1412.6980>
  - [34] Z. Wu, A. Schmidt, R. Moore, H. Zhou, A. Banks, P. Kazanzides, and S. E. Salcudean, “Surgipose: a dataset for articulated robotic surgical tool pose estimation and tracking,” in *2025 IEEE International Conference on Robotics and Automation (ICRA)*, 2025, pp. 10 507–10 514.
  - [35] N. Ravi, J. Reizenstein, D. Novotny, T. Gordon, W.-Y. Lo, J. Johnson, and G. Gkioxari, “Accelerating 3d deep learning with pytorch3d,” *arXiv:2007.08501*, 2020.
  - [36] J. Shi and Tomasi, “Good features to track,” in *1994 Proceedings of IEEE Conference on Computer Vision and Pattern Recognition*, 1994, pp. 593–600.
  - [37] L. G. Rosenzweig, B. Shacklett, W. Xia, and K. Fatahalian, “High-throughput batch rendering for embodied ai,” in *SIGGRAPH Asia 2024 Conference Papers*, ser. SA ’24. New York, NY, USA: Association for Computing Machinery, 2024. [Online]. Available: <https://doi.org/10.1145/3680528.3687629>